Proceedings of the 2015 ASME International Mechanical Engineering Congress and Exposition
IMECE2015
November 13-19, 2015, Houston, Texas USA

IMECE2015-52529

Application of Microscale Devices for Megawatt Scale Supercritical Carbon Dioxide Concentrating Solar Power Receivers

Kyle R. Zada
Oregon State University
Corvallis, Oregon, USA

M. Kevin Drost
Oregon State University
Corvallis, Oregon, USA

Brian M. Fronk
Oregon State University
Corvallis, Oregon, USA

ABSTRACT

Concentrated solar power (CSP) plants have the potential to reduce the consumption of non-renewable resources and greenhouse gas emissions in electricity production. In CSP systems, a field of heliostats focuses solar radiation on a central receiver, which is ultimately transferred to thermal electrical power plant at high temperature. However, the maximum receiver surface fluxes are low (30–100 W cm^{-2}) with high thermal losses, which has limited the market penetration of CSP systems.

Recently, small (~ 4 cm^2), laminated micro-channel devices have shown potential to achieve concentrated surface fluxes over 100 W cm^{-2} using supercritical CO_2 as the working fluid. The present study explores the feasibility of using these microscale devices as building blocks for a megawatt scale (250 MW thermal) open solar receiver. This allows for a modular design of the central receiver with non-standard shapes customized to the heliostat field. The results show that the microscale unit-cells have the potential to be scaled to megawatt applications while providing high heat flux and thermal efficiency. At the design incident flux and surface emissivity, a global receiver thermal efficiency of > 90% can be achieved.

NOMENCLATURE

A	Area (m^2)
C	Flow over tubes correlation coefficient (-)
D	Diameter (m)
G	Incident flux (W cm^{-2})
	Mass Flux (kg m^{-2} s^{-1})
Gr	Grashoff Number (-)
h	Heat transfer coefficient (W m^{-2} K^{-1})
	Enthalpy (J kg^{-1})
k	Thermal conductivity (W m^{-1} K^{-1})
L	Characteristic length (m)
LMTD	Log-mean temperature difference (K)
$\dot{m}$	Mass flow rate (kg s^{-1})
Nu	Nusselt number (-)
P	Pressure (bar)
$\dot{Q}$	Heat transfer rate (W)
Pr	Prandtl number (-)
R	Thermal resistance (K W^{-1})
Re	Reynolds number (-)
S	Pin Pitch (μm)
T	Temperature (°C)
U	Overall HTX coefficient (W m^{-2} K^{-1})
V	Velocity (m s^{-1})
W	Height (m)

Greek Symbols

α	Absorptivity (-)
ε	Emissivity (-)
η	Thermal Efficiency (-)
ρ	Density (kg m^{-3})
μ	Dynamic Viscosity (kg m^{-1} s^{-1})

Subscripts and Superscripts

Air	External Air
Amb	Ambient
BW	Base Width of Unit Cell
Conv	Convection
C	Critical
D	Diagonal
Ext	External
F /Forced	Forced Convection
Free	Natural Convection
H	Hydraulic
Int	Internal
lam	Laminar
L	Length
Loss	Losses from unit cell/module
m	Flow over tubes correlation coefficient
max	Maximum value
min	Minimum value
Pin	Pin
Pin Surf	Pin-fin surface
r	Radiation
s	Surface
sCO_2	Supercritical carbon dioxide
Solar	Solar energy
T	Transverse
Tot	Total
turb	Turbulent

INTRODUCTION

Concentrating solar power (CSP) systems have the potential for centralized, carbon free electricity generation. A CSP system, in essence, is a field of sun-tracking mirrors, called heliostats, which concentrate solar energy on a central receiver [1]. Here, a working fluid is heated by the incident solar flux and is then either directly utilized or functions as the thermal source for a Rankine or Brayton cycle to produce electricity.

The central receiver is a key cost driver of CSP systems [2]. Current receiver technology in CSP systems are able to absorb incident solar flux on the order of 30–100 W cm^{-2} [2,3]. To compete with fossil-fuel and other renewable energy sources, CSP systems need to be able to absorb higher incident flux (>100 W cm^{-2}) with high efficiencies (> 90%). This will reduce the receiver size for a given plant capacity and ultimately decrease the cost per kWh of electricity [2,3]. To achieve this, recent efforts have focused on using supercritical carbon dioxide (sCO_2) as the working fluid in high-temperature solar receivers for CSP [4–7]. Supercritical CO_2 offers favorable thermosphysical properties, good volumetric efficiency (yielding smaller volume components) and is capable of stable operation at high temperatures > 600°C. The sCO_2 heated in a central receiver can be directly utilized in a supercritical Brayton cycle.

A sCO_2 central receiver must be capable of high incident flux at high temperature and pressure (> 200 bar). Devices using microscale geometries (D_H ~ 500 μm) have the coupled advantage of providing high heat transfer coefficients and small fluid volumes to mitigate high pressure concerns. Microscale pin-fin geometries have received significant interest in the literature for their ability to absorb or reject high surface fluxes, particularly in computer chip cooling, high power electronics cooling and compact chemical reactors [8]. However, scaling of these micro devices to a large, megawatt scale solar receiver presents several challenges.

Full-scale testing of central receiver facilities is costly and time-consuming; analytical modeling of these devices is of interest for rapid investigation of performance of a sCO_2 receiver. Previous efforts on receiver design and optimization have focused on numerical models [9–13] for molten salts and other working fluids. These models incorporate CFD techniques to simulate performance with static and dynamic solar loading and different experimental receivers. Although full CFD simulation provide detailed and accurate results of thermal-fluidic performance under varying operational conditions, implementing CFD modeling for a full scale, solar receiver would require a large amount of computation power, time and cost, inhibiting rapid parametric evaluation of different design variables.

The present study investigates the potential of leveraging the enhanced heat transfer of microscale devices through the development of a computationally efficient, multi-scale, analytical model of a sCO_2 central receiver. The analytical model allows quick evaluation of receiver performance trends and parametric analysis of different receiver configurations. The results of the models prove the potential for sCO_2 receivers built on microscale devices. Furthermore, the model can be used to narrow the envelope of design parameters before a full transient, computational analysis is performed.

The basic design of the central multi-scale solar receiver under consideration is shown in Figure 1. Here, several flat plate modules (~ 1 m^2) are combined to form a large surface area receiver. Each module consists of individual microchannel unit cells plumbed in parallel. By increasing the heat transfer coefficient of the working fluid with the microscale features, a smaller receiver is able to accommodate an increase in incident solar flux and therefore significantly reduces the size, cost, and thermal losses of the receiver.

MODELING APPROACH

Recent numerical [14] and experimental [15] work conducted at Oregon State University has shown the potential for small (~4 cm^2), laminated micro-channel receivers to be capable of handling concentrated solar fluxes up to 100 W cm^{-2} with thermal efficiencies greater than 95% (excluding reflection losses, as defined by Eq. 1), using supercritical CO_2 as the working fluid. This work has focused on individual microscale unit cells and has not addressed the issues in "numbering up" the

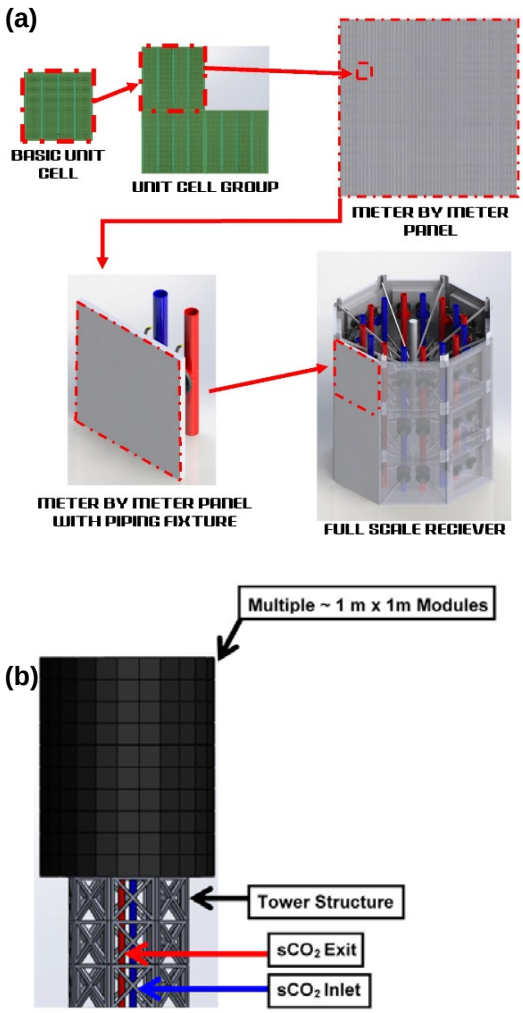

Figure 1: Illustration (a) of Unit Cell Concept and (b) Full Receiver Tower

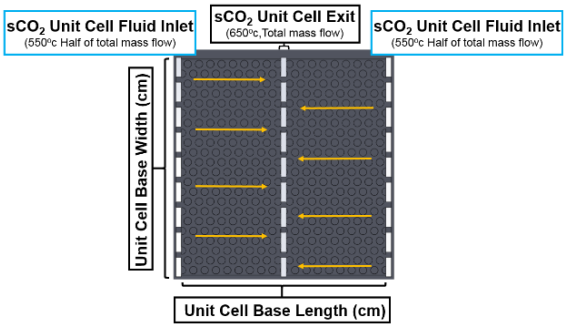

Figure 2: Unit Cell Geometry.

microchannel unit cells to a full scale commercial receiver (~ 250 MW thermal).

$$\eta_{Thermal} = \frac{\left(\dot{Q}_{sCO2}\right)}{\left(G_{solar} \times A_S \times \alpha\right)} \quad (1)$$

The present study uses the results from Rymal *et al.* and L'Estrange *et al.* [14,15] to guide the development of an analytical model of a full scale central receiver system using multiple microscale pin-fin devices. The proposed commercial receiver is a modular, multiscale design (with a conceptual design shown in Figure 1). It consists of numerous 1 m^2 receiver modules, which are in turn composed of smaller high-flux microchannel unit cells. Heat transfer and pressure drop network submodels for the individual unit cell and 1 m^2 module were developed. These submodels were then integrated into a commercial receiver model. Together, the overall receiver and individual module thermal efficiency were determined for varying incident flux, ambient conditions and central receiver layouts. This proposed design allows for high microchannel heat transfer rates while maintaining low pressure drops across the pin-fins, enabling greater incident flux and thermal efficiencies than conventional central receiver designs, reducing size and cost.

The receiver design under consideration uses sCO_2 as the working fluid. The mass flow rate per 1 m^2 module is controlled to provide an exit temperature of 650°C with an inlet temperature of 550°C and operating at an internal pressure of 200 bar.

UNIT CELL MODEL DEVELOPMENT

The lowest level submodel in the commercial receiver design is the unit cell. From previous work [14,15] it was determined that an optimal unit cell geometry would consist of small pins in a staggered array which increases the heat transfer to the sCO_2 while still maintaining a relatively low pressure drop.

A schematic of the pin-fin geometry is provided in Figure 2. Here, the sCO_2 fluid enters the unit cell at both the left and right edge slots at a temperature of 550°C and pressure of 200 bar. Supercritical CO_2 flows through the staggered pin arrays absorbing the incident flux, and then exits the unit-cell at a temperature of 650°C through the center of the unit cell.

Important dimensions of the unit cell are summarized in Table 1. The pin-fin array is covered with a thin (580μm) flux plate to minimize conduction resistance. The internal pin geometry modeled here is almost identical to the unit cell experimentally characterized examined in L'Estrange *et al.* [15], with a 700 μm pin diameter, pin height of 360 μm, diagonal and longitudinal pitch of 1050 μm, and transverse pitch of 1820 μm as seen in the close up schematic in Figure 3.

To accommodate the high working temperature and pressure, the unit cell is constructed of Haynes 230 Ni-Cr alloy [16], coated with a highly absorptive surface ($\alpha = 0.95$). For this study, the base length of the unit-cell was assumed to be 8 cm, with the base width held at 1 m (see Figure 2). Thus, a total of twelve unit cells configured in parallel would yield approximately a 1 m × 1 m panel surface (0.96 m^2). Over the exterior surface of the unit-cell, a 2 m s^{-1} wind velocity is induced to simulate forced convection around the central receiver system.

The primary outputs of the unit cell model required for input into the module and full receiver models are the total energy absorbed by the sCO_2, and the mass flow per unit cell required for a fluid temperature rise of 100 K (from 550 to 650°C). Representative results are presented in this section for a 1 m × 0.08 m until cell with an incident flux of 110 W cm^{-2}, air velocity of 2 m s^{-1} and an ambient temperature of 20°C. A surface energy balance yields the following relation for total rate of energy transferred to the sCO_2:

$$\dot{Q}_{sCO2} = G_{solar}\alpha A_s - \dot{Q}_{loss} \quad (2)$$

A system of equations was developed to calculate each term in Eq. 2 by accounting for the multi-mode heat transfer effects of radiation, convection, and conduction, as seen in Figure 4. The model was developed using the *Engineering Equation Solver* (EES) platform [17]. Unless otherwise noted, all fluid properties are evaluated at the bulk average fluid temperature either between the unit cell exterior surface temperature and ambient or between the inlet/exit of the pin-fin geometry. The external air properties are evaluated from the equation-of-state, as defined by Lemmon *et al.* [18] while the internal carbon-dioxide

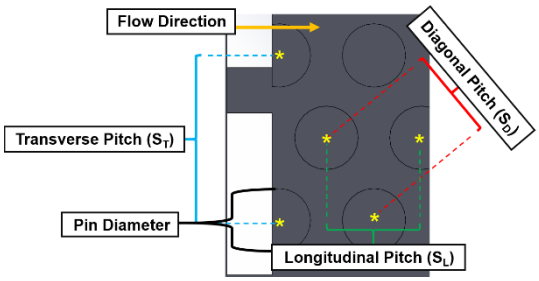

Figure 3: Pin-Fin Geometry.

Table 1: Unit Cell Pin-Fin Geometry.

Coversheet Thickness	580 μm
Pin Diameter	700 μm
Pin Height	360 μm
Longitudinal Pitch	1050 μm
Transverse Pitch	1820 μm
Diagonal Pitch	1050 μm

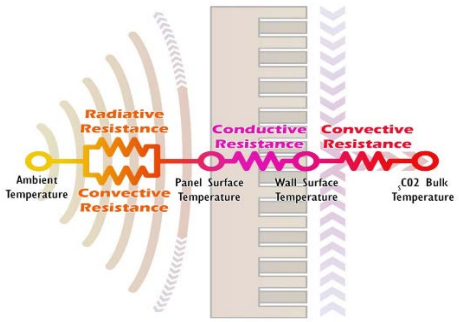

Figure 4: Thermal Resistance Model.

properties are evaluated from the equation-of-state, as defined by Span and Wagner [19].

The surface temperature (T_s) of each unit cell was assumed to be uniform. The radiative resistance (Eq. 3) was calculated as a function of the radiative resistance heat transfer coefficient (Eq. 4).

$$R_{\text{Rad Ext}} = \frac{1}{h_{\text{rad}} \times A_S} \tag{3}$$

$$h_{rad} = \varepsilon \times \sigma \left(T_S + T_{Amb}\right) \times \left(T_S{}^2 + T_{Amb}{}^2\right) \tag{4}$$

Here, the ambient temperature was assumed constant at T_{amb} = 20°C, the panel surface emissivity (ε) was 0.95 and the unit-cell surface area (A_s) was 0.08 m^2 (for the nominal 0.08 × 1 m unit cell). For the representative case, h_{rad} = 67 W m^{-2} K^{-1} and $R_{\text{rad, ext}}$ =0.1865 K W^{-1}.

Convection heat transfer was modeled assuming a vertical flat plate geometry for each unit cell. Losses were attributed to forced, free, or a combination of both depending the ratio of Grashoff Number (buoyancy induced flow) to Reynolds Number (forced induced flow), with the criteria provided in Table 2.

For forced convection, the Reynolds number was determined as a function of the external air density(ρ_{ext}), wind speed (V_{ext}), characteristic length (L_{Char}) (defined as the *module* length = length unit cell × # unit cells per module), and the external air dynamic viscosity (μ_{air}), where the fluid properties are evaluated at the average film temperature between the ambient and unit cell surface.

The forced convection heat transfer coefficient was modeled using the laminar and turbulent correlations developed by Kays *et al*. (as reported in Bergman *et al*. [20], Eqs. 5 and 6).

Table 2: Convection Loss Criteria.

$\left(\frac{Gr_{air}}{Re_{air}{}^2}\right) \approx 1$	$Nu_{Total}{}^N = Nu_{Free}{}^N + Nu_{Forced}{}^N$ N = 3
$\left(\frac{Gr_{air}}{Re_{air}{}^2}\right) < 1$	$Nu_{Total} = Nu_{Forced}$
$\left(\frac{Gr_{air}}{Re_{air}{}^2}\right) > 1$	$Nu_{Total} = Nu_{Free}$

$$Nu_{F\ Lam} = 0.456\left(Re_{Air}{}^{1/2}\right)\left(Pr_{Air}{}^{1/3}\right) \tag{5}$$

$$Nu_{F\ Turb} = 0.0308\left(Re_{Air}{}^{4/5}\right)\left(Pr_{Air}{}^{1/3}\right) \tag{6}$$

where the Prandlt number is evaluated at the film average air temperature between the ambient and unit cell surface [21].

The free convection Nusselt number was calculated from a correlation developed by Churchill and Chu [22], where the characteristic length was the unit cell width (*i.e.*, vertical dimension).

$$Nu_{Free} = \left(0.825 + \frac{\left[\left(0.387 \cdot Ra_{Air}{}^{1/6}\right)\right]}{\left(1 + \left(0.492/Pr_{Air}\right)^{9/16}\right)^{8/27}}\right)^2 \tag{7}$$

The total external convection resistance was then determined using the external convection coefficient and the panel exterior surface area.

$$R_{Conv\ Ext} = \frac{1}{h_{Conv\ Air} \cdot A_S} \tag{8}$$

For the sample case, natural convection was determined to be the governing mechanism, with a natural convection Nusselt number of 159.5 and a convective resistance, $R_{\text{conv,ext}}$ = 1.7 K W^{-1}.

Combining the effects of radiation and convection in parallel, the overall exterior heat transfer conductance was found from the inverse of the total exterior heat transfer resistance.

$$UA_{Ext} = \frac{1}{R_{Ext\ Tot}} \tag{9}$$

Newton's Law of cooling was used in conjunction with the surface temperature (determined via iteration as T_s = 681 °C for the sample case), ambient temperature, and the overall exterior heat transfer coefficient to determine the total exterior heat losses from the panel surface.

$$\dot{Q}_{\text{loss}} = UA_{Ext} \cdot \left(T_S - T_{Amb}\right) \tag{10}$$

The calculated loss for the sample case was 3,946 W (convection and radiation). The rate of heat transfer from the panel surface to the sCO_2 was a function of the conduction resistance of the thin flux cover plate and the convection thermal resistance of the sCO_2 in the micro-pin fin array. The conduction resistance is determined using the panel coversheet thickness(L_{Cover}), coversheet thermal conductivity (k_{Cover}), and exterior panel surface area (A_S). The internal convection resistance ($h_{\text{conv,sCO2}}$ = 19,370 W m^{-2} K^{-1} and $R_{\text{conv, sCO2}}$ = 0.00055 K W^{-1} for the representative case) is determined using the internal sCO_2 heat transfer coefficient and the pin-fin/base surface area.

$$R_{Conv\ sCO2} = \frac{1}{h_{Conv\ sCO2} \times A_{Pin\ Surf}} \quad (11)$$

The pin-fin efficiency was used to determine the effective pin heat transfer area, and was dependent upon the pin diameter, pin height, sCO_2 heat transfer coefficient, and pin thermal conductivity, with a range between 69.8 to 83.7% in efficiency depending on the mass flow rate of sCO_2 (and the associated convective heat transfer coefficient).

Convective heat transfer correlations in the literature for micro pin-fin geometries have been primarily developed for single-phase, laminar flows [23,24] In the present study, the supercritical CO_2 is expected to be highly turbulent, with Reynolds number greater than 10,000, well outside the range of applicability for available pin-fin correlations. Attempts to use the correlations developed for laminar flow in pin arrays yielded physically unrealistic results. Thus, the heat transfer coefficient of the sCO_2 flow through the pin-fins, was approximated using a conventional model for flow over a bank of tubes (Zukauskas [25]).

The minimum transverse flow area in the pin-fin geometry is first determined as a function of diagonal pitch (S_D), diameter of the pin-fins (D_{fin}) and the transverse pitch (S_T) of the geometry, as seen in Figure 3.

$$A_{min} = \frac{2\left(S_D - D_{fin}\right)}{S_T}\left(W_{pin} L_{BW}\right) \quad (12)$$

This particular flow area is for a staggered pin-fin array where the following relationship is valid:

$$\frac{S_T + D_{fin}}{2} > S_D \quad (13)$$

The maximum mass velocity (G_{Max} = 2,300 kg m^{-2} s^{-1} for the sample case) of the sCO_2 fluid is then used to define the pin-fin Reynolds number with the pin-diameter as the length parameter.

$$G_{max} = \frac{\dot{m}_{min}}{A_{min}} \quad (14)$$

$$\mathrm{Re} = \frac{\left(G_{Max}\right)\left(D_{fin}\right)}{\mu_{sCO_2}} \quad (15)$$

The Reynolds number and the Prandtl number are then then used to find the Nusselt number from the correlation developed by Zukauskas [25] (Eq. 16). The 'C_1' and the 'm' parameters are defined as $0.35(\frac{S_T}{S_L})^{1/5}$ and 0.60, respectively, for the given operating geometry [20,25]. The parameter (Pr_s) is the Prandtl number evaluated at the pin-fin base fluid temperature while the other properties are evaluated at the bulk average sCO_2 fluid temperature.

$$Nu_{sCO_2} = \left(C_1\right)\left(Re_{sCO_2}\right)^m (\mathrm{Pr})^{0.36}\left(\frac{\mathrm{Pr}}{\mathrm{Pr}_s}\right)^{0.25} \quad (16)$$

Combining the effects of conduction and convection in series, the overall internal conductance was determined by taking the inverse of the total internal resistance.

$$UA_{Int} = \frac{1}{R_{Int\ Tot}} \quad (17)$$

The Log-Mean-Temperature-Difference (LMTD Eq, 18.) was then used to determine the amount of heat absorbed into the flow sCO_2:

$$LMTD = \frac{\left(T_S - T_{sCO2\ Exit}\right) - \left(T_S - T_{sCO2\ Inlet}\right)}{\left(\log\frac{\left(T_S - T_{sCO2\ Exit}\right)}{\left(T_S - T_{sCO2\ Inlet}\right)}\right)} \quad (18)$$

Here, the surface temperature is assumed uniform and the inlet and outlet sCO_2 temperatures were specified. Finally, the mass flow rate of the sCO_2 is required to determine the internal convection heat transfer coefficient. Closure to the system of equations and the required mass flow rate was obtained from an energy balance on the unit cell.

$$\dot{m}_{sCO_2} = \frac{\left(Q_{sCO_2}\right)}{\left(h_{sCO_2\ Exit} - h_{sCO_2\ Inlet}\right)} \quad (19)$$

As a performance metric, the thermal efficiency of the pin-fin module is defined as the amount of heat transferred to the sCO_2 compared to the amount of incident energy that was available on the panel surface, disregarding the reflection losses (see Eq. 1). This parameters is a direct *thermal* performance metric of the pin-fin geometry without accounting for the surface coatings, as discussed in L'Estrange *et al*. [15]. For the sample case, the mass flow rate of sCO_2 was 0.32 kg s^{-1} and the thermal efficiency was 95.3%. During a parametric evaluation of unit cell size, the sCO_2 heat transfer coefficient ranges between 5,430 W m^{-2} K^{-1} and 88,300 W m^{-2} K^{-1}, Reynolds number between 5,000 and 520,100 and LMTD between 158.9K and 38.1K for unit cells of 1 cm × 1 cm and 100 cm × 100 cm, respectively. The results of the unit cell model were used as inputs to the module level model, discussed below.

MODULE LEVEL MODEL

The single module model implements the exact same methodology as the single unit cell model, with the total number of unit cells per module specified by the user. Data from each individual unit cell model run was recorded, and the overall incident solar flux, heat input to the sCO_2, and external heat loss was determined at the module level by summing the value of each parameter from the individual unit cell models. The total module efficiency is determined by taking the total absorbed solar flux into the sCO_2 versus the amount of total incident flux,

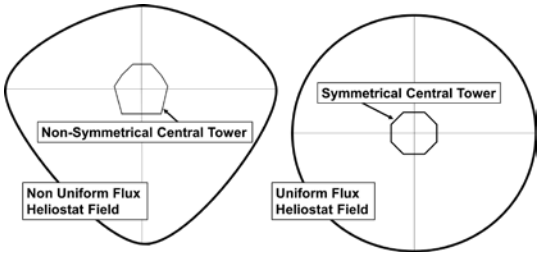

Figure 5: Receiver Tuned to Heliostat Field.

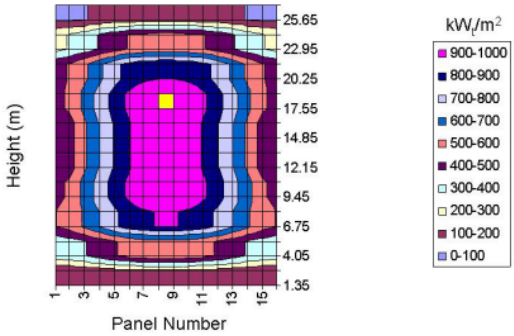

Figure 6: Non-Uniform Flux Model, *DELSOL* Modeling [3]**.**

disregarding the solar flux losses in the form of reflection. The global results of each module model were then used in the development of the commercial receiver model.

COMMERCIAL RECEIVER MODEL

The full scale commercial receiver model was developed as a composite of both the single unit cell and module models. In the proposed commercial receiver design, modules are mounted to a central structure, which can be arranged in a variety of different shapes. Supercritical CO_2 is delivered, as was shown previously in Figure 1, to each panel module, where it is then further subdivided to each unit cell.

The modular design allows for the potential of unconventional central receiver geometries (compared to a standard cylinder) as seen in Figure 5, allowing the receiver shape to be tuned to heliostat fields with non-uniform flux.

To evaluate the performance of the receiver system in an actual heliostat field, a representative circumferential variation of flux distribution equation was developed. An representative non-uniform distribution of incident flux was developed by Kolb [3] using the DELSOL heliostat field modeling software, shown in Figure 6.

For this particular model, it can be seen that there is a drastic decrease in incident solar flux from the northern facing panels (8 and 9) to the southern facing panels (1 and 15) with a drop in incident solar flux on the order of approximately 53%. Using this distribution as the basis, a scaled non-uniform flux distribution was developed for the current study with a 53% drop in incident flux from the northern to southern panels (circumferentially) and a peak flux of 110 W cm^{-2}, as seen in Figure 7. The vertical change in incident flux was assumed negligible. The full receiver model allows the effect of changes in geometry (from the micro-pin unit cell to the layout of the full receiver) on the thermal performance to be understood. The model can also be used as a design tool to tailor the global receiver shape to different heliostat fields.

RESULTS AND DISCUSSION

Numerous parameters including surface temperature, thermal efficiency, heat transfer to the sCO_2, and sCO_2 mass flow rate were determined using the developed models at the individual unit cells, module and the entire receiver level. Although the pin-fin geometry is held constant, the unit-cell base length and unit-cell base width can be adjusted to understand the effect of different unit cell sizes on thermal efficiency. The analytical model unit cell model was first validated by comparing the results with the experimental work of L'Estrange *et al*. [15]. In their study, a 2 cm × 2 cm unit cell was used. Then, the unit cell model was evaluated at the design condition of 1 m × 8 cm at varying incident flux.

Next, the module level design was evaluated. Two cases were considered, the performance of a module comprised of 12 parallel 1 m × 8 cm unit cells and a module consisting of a single 1 m × 96 cm unit cell. Finally, the commercial scale receiver model was used to evaluate three different commercial receiver designs.

Unit-Cell Model Validation (2 cm × 2 cm)

For a single 2 cm × 2 cm pin-fin micro-channel panel, the efficiency of the panel was determined as a function of incident flux between 20 W cm^{-2} and 200 W cm^{-2}, as seen in Figure 8.

The efficiency of the 2 cm × 2 cm unit cell is very sensitive to a reduction incident surface fluxes. This can be attributed to the design requirement that a constant sCO_2 temperature lift is maintained. At lower fluxes, the mass flow rate is reduced to maintain the temperature difference, which yields a reduction in internal convective heat transfer coefficient and overall efficiency.

The analytical results here are consistent with the experimental work conducted by L'Estrange *et al*. [15]. They showed that the efficiency of a similar 2 cm × 2 cm unit is constant, for incident fluxes between 70 – 120 W cm^{-2}, at approximately 94%. As seen in Figure 8, for incident fluxes

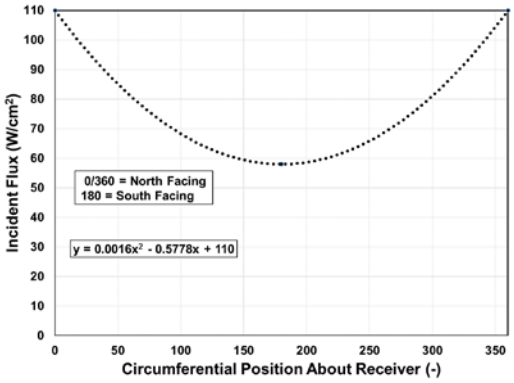

Figure 7: Non-Uniform Surface Flux from Heliostat Field.

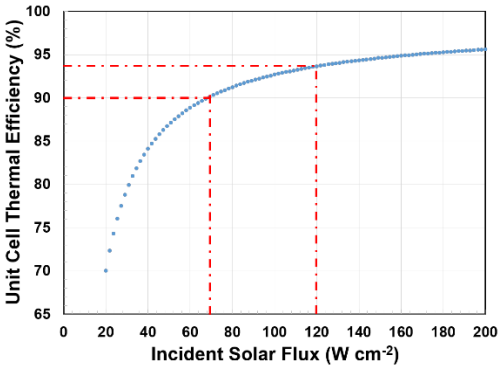

Figure 8: Validation Unit Cell Thermal Efficiency versus Incident Solar Flux.

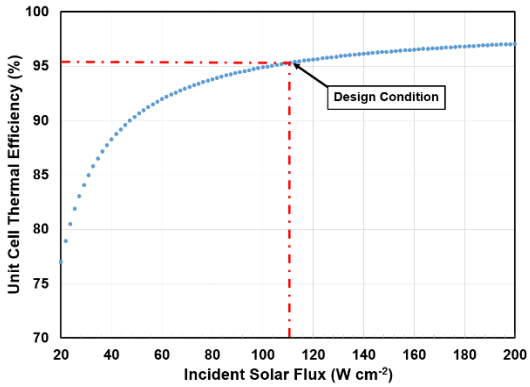

Figure 9: Module Unit Cell Thermal Efficiency versus Incident Solar Flux.

between 70 - 120 W cm^{-2}, the panel efficiency varies between 90 and 94%.

Single Unit Cell (1 m × 8 cm) Analysis

Adjusting the unit-cell to a 1 m cross-flow length and 8 cm flow length, there will be an increase in surface area of the individual unit cell. In doing so, the total amount of energy that can be absorbed will increase (assuming constant flux), which will result in an increase in the total sCO_2 mass flow rate (for a fixed temperature difference) and internal heat transfer coefficient. The efficiency is again very sensitive at lower incident fluxes, however, as the incident flux increases beyond 100 W cm^{-2}, the efficiency begins to approach approximately steady-state in efficiency between 95% and 97%, as seen in Figure 9.

For this geometry, increasing the incident flux by a factor of two (100 W cm^{-2} to 200 W cm^{-2}), the efficiency is only increased by two percentage points.

The effect of the external energy loss is important to understand which mode(s) of heat loss are dominant for a vertical panel surface. As the incident flux on the module increases, the external heat loss will increase due to the rise in surface temperature and the associated radiation and convection losses. The relative contribution of convective and radiation losses as a function of incident flux are shown in Figure 10.

With an increase in incident surface flux, the convection heat loss is relatively constant while the re-radiation heat loss increases with increasing incident flux. At a peak of incident flux

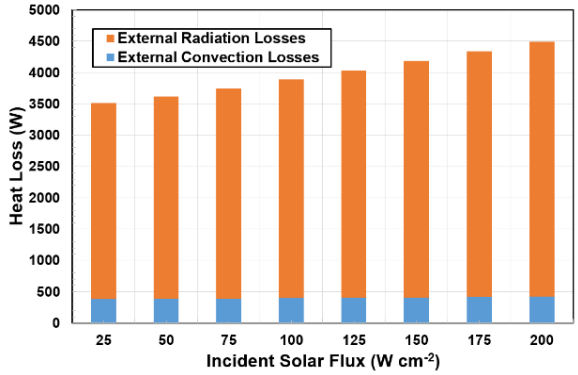

Figure 10: Module Unit Cell Convection and Radiation Losses versus Incident Solar

(200 W cm^{-2}), the heat loss in the form of re-radiation increases by 35% from a minimum incident flux (20 W cm^{-2}). Radiation dominates the heat loss from the exterior of the module surface**.**

Single Module Analysis

Using a unit cell with a 1 m cross-flow length and an 8 cm flow length, a total of 12 individual unit cells are used in parallel to create ~ 1 m^2 module surface. An alternative option is to not implement the arrayed unit cells but rather use a single unit cell with dimensions of 1 m long by 0.96 m wide (*i.e.*, a surface area equivalent to twelve 1 m × 0.08 m unit cells). The cell width is the same for both cases (1 m), thus the sCO_2 flow face area (see Figure 2) is the same. Since the total flux incident on the 0.96 m^2 module is the same between the two cases, the mass flow for the single unit cell is approximately 12 times that of the individual unit cells to achieve the specified 100 K change in temperature. This will lead to a significantly higher velocity over a longer flow length, increasing heat transfer coefficient and yielding undesirable pressure drop.

To highlight the utility of the unit cell approach, a comparison is made between these two module designs to investigate the performances between a module that contains arrayed unit cells and a module consisting of a single large unit cell.

The internal sCO_2 heat transfer coefficient and module efficiency for each module surface type are compared, as seen in Figure 11. As expected, the internal heat transfer coefficient for the module without unit cells is much larger than the module with unit cells.

However, the use of a single-unit cell results in significantly increased pressure drop due to both increased mass flow rate and increased flow length. Using the Churchill friction factor in conjunction with the Darcy Weisbach pressure drop equation [26], the pressure drop for the single cell would be more than 100% of the operating pressure, while for the multiple unit cell the pressure loss is calculated as less than 4% of the absolute pressure. Therefore, optimizing the unit cell to achieve an increased heat transfer coefficient while minimizing the pressure drop is crucial to the module efficiency and overall performance.

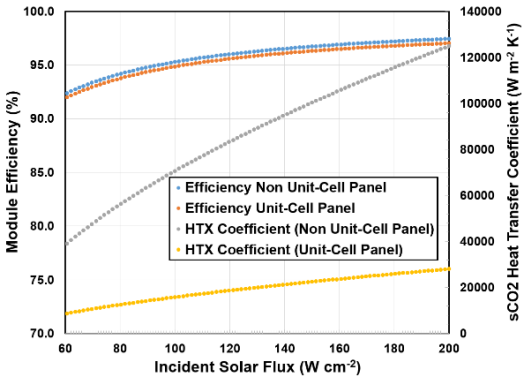

Figure 11: Module Performance Comparison, with and without Unit Cells.

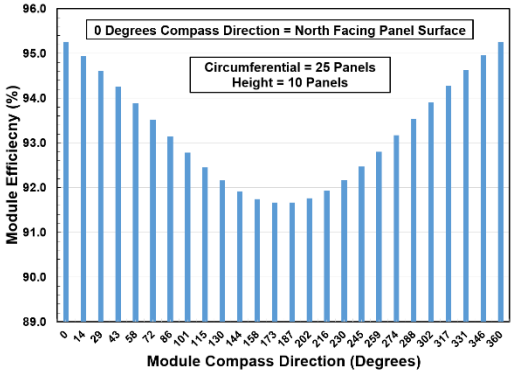

Figure 13: Module Thermal Efficiency versus Compass Direction.

Full Scale Receiver Results

One of the advantages of the proposed modular central receiver design is that the shape of the receiver can be customized to a given heliostat field. To explore this, three different central receiver module configurations were investigated. Each design had the same number of modules (*i.e.*, equivalent surface area) and were 10 modules in height (~ 10 m). The baseline design is a cylindrical collector with 25 panels circumferentially, subjected to a non-uniform flux distribution as detailed previously (see Figure 12).

The baseline module efficiencies, which are dependent upon the circumferential direction of the module, can be seen in Figure 13. Since a uniform flux distribution was assumed in the vertical direction a single layer of modules is sufficient for evaluating the global trend.

The northern-facing panels have the highest panel efficiencies of ~95.3% while the southern-facing panels have the lowest panel efficiencies with ~91.6%. Overall, as seen in Table 3, the cylindrical receiver is able to absorb 160 MW into the sCO_2 with an overall efficiency of 93.6%.

The second receiver design has 8 panels on the north-facing side with 5 panels on the south-facing side with 6 panels on each connecting side, as seen in Figure 14.

With an increase in the number of northern-facing panel surfaces, the collector surface area becomes more effective. The non-cylindrical design 1 is able to absorb 168.9 MW into the sCO_2 at an efficiency of 93.6%, as seen in Table 4. This is an increase of 5% in absorbed energy from the cylindrical receiver design with the same surface area.

Table 3: Cylindrical Receiver Performance, 250 Modules

Total Receiver Incident Flux	181.0 MW
Total Receiver Heat Input sCO_2	160.7 MW
Total Receiver Reflection Losses	9.0 MW
Total Receiver Heat Losses	11.3 MW
Overall Receiver Efficiency	93.4%

The third investigated collector has 11 panels on the North-facing side with 4 panels on the South-facing side with 5 panels on each connecting side, as seen in Figure 15.

Overall, as seen in Table 5, the non-cylindrical design 2 is able to absorb 176 MW of energy into the sCO_2 at an efficiency of 93.9%. This is an increase of ~8.8% in absorbed energy from the cylindrical receiver design.

CONCLUSIONS

This study investigates the feasibility of using microscale devices as the building blocks for a megawatt scale open receiver for solar thermal power generation.

An analytical model was developed using multi-mode effects of heat transfer on the exterior and internal components of the receiver module. A comparison with experimental results of a 2 cm × 2 cm unit cell showed agreement with a 2 cm × 2 cm analytical model within 4% in efficiency.

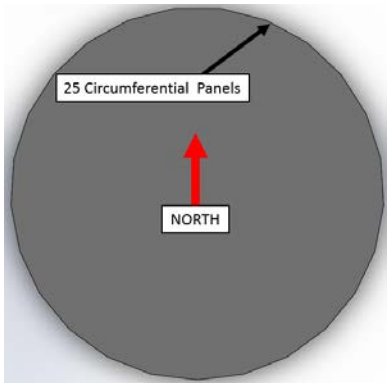

Figure 12: Cylindrical Receiver, 25 Circumferential Modules.

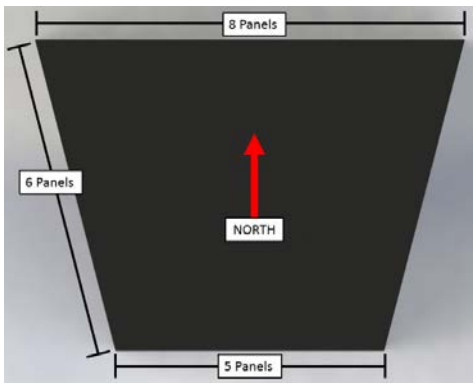

Figure 14: Modified Receiver Design #1.

Table 4: Modified Receiver # 1 Performance, 250 Modules.

Total Receiver Incident Flux	189.8 MW
Total Receiver Heat Input sCO_2	168.9 MW
Total Receiver Reflection Losses	9.5 MW
Total Receiver Heat Losses	11.4 MW
Overall Receiver Efficiency	93.6%

A larger unit cell (1 m × 8 cm) increases the overall absorbed solar flux and efficiency. The efficiency of the unit cell stabilizes with an incident flux beyond 100 W cm^{-2}; increase in incident flux causes an increase in surface temperature and likewise exterior heat losses.

Combining the unit cells together to create a full ~ 1 m^2 module will have a lower internal sCO_2 heat transfer coefficient as compared to a full panel with pin-fin architecture. Pressure drop for flow through a pin-fin geometry are constrained by the flow length of the module. A full module without unit cells would have an unrealistic pressure drop in a commercial scale device; the unit cells are able to allow for lower pressure drops while still maintaining high efficiency and absorbed solar flux. Future analysis of the pressure drop is required to optimize the unit cell for an individual module by accounting for the pressure drop not only through the pin-fin array but through flow through piping networks to supply the sCO_2 to the unit cell.

Three central receiver configurations have been investigated (multi-sided cylinder and two four-sided polygons) and the variation in the global and local thermal efficiency of each unit is explored. At the design non-uniform incident flux and surface emissivity, a global receiver thermal efficiency of >90% can be achieved for all three designs. With an increase in northern-facing panels, while still keeping the total surface area constant, the absorbed solar thermal energy can be increased while also increasing the receiver efficiency. Overall, a receiver built with individual modules has shown the ability to be tailored to adapt to a non-uniform field flux to achieve consistent efficiency and sCO_2 delivery temperature throughout the receiver.

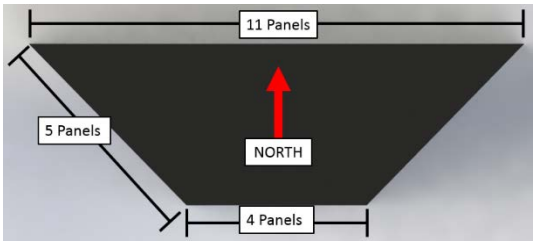

Figure 15: Modified Receiver Design #2.

Table 5: Modified Receiver # 2 Performance, 250 Modules.

Total Receiver Incident Flux	197.4 MW
Total Receiver Heat Input sCO_2	176.1 MW
Total Receiver Reflection Losses	9.9 MW
Total Receiver Heat Losses	11.4 MW
Overall Receiver Efficiency	93.9%

Future work for this study would entail verifying the accuracy of the sCO_2 heat transfer coefficient calculation in the analytical model with experimental validation and optimizing the size of unit cell for commercialized use with constraints due to pressure drop. The heat transfer coefficient ultimately determines the efficiency of the solar absorption into the sCO_2, and therefore represents the efficacy of using this technology for solar thermal energy applications. An over or under approximation for the heat transfer coefficient can yield an inaccurate value of thermal efficiency. Since the unit cell is the base device in the overall receiver, optimization of size will allow for more effective heat transfer to the working fluid, increase efficiency, and overall decrease cost by minimizing the amount of unit cells per module. Pressure drop across the pin-fin architecture is of importance for commercialization of an actual module, and therefore needs to be properly modeled for optimization of the unit cell size.

REFERENCES

[1] Stine, W., and Geyer, M., 2001, "Power From the Sun."

[2] Romero, M., Buck, R., and Pacheco, J. E., 2002, "An Update on Solar Central Receiver Systems, Projects, and Technologies," J. Sol. Energy Eng., **124**(2), p. 98.

[3] Kolb, G. J., 2011, An Evaluation of Possible Next-Generation High-Temperature Molten-Salt Power Towers, Albuquerque, NM.

[4] Turchi, C. S., Ma, Z., Neises, T. W., and Wagner, M. J., 2013, "Thermodynamic Study of Advanced Supercritical Carbon Dioxide Power Cycles for Concentrating Solar Power Systems," J. Sol. Energy Eng., **135**(4), p. 041007.

[5] Ma, Z., and Turchi, C., 2011, "Advanced supercritical carbon dioxide power cycle configurations for use in concentrating solar power systems," Supercritical CO2 Power Cycle Symposium, Boulder, CO, USA.

[6] Singh, R., Miller, S. a., Rowlands, A. S., and Jacobs, P. a., 2013, "Dynamic characteristics of a direct-heated supercritical carbon-dioxide Brayton cycle in a solar thermal power plant," Energy, **50**(1), pp. 194–204.

[7] Chacartegui, R., Muñoz De Escalona, J. M., Sánchez, D., Monje, B., and Sánchez, T., 2011, "Alternative cycles based on carbon dioxide for central receiver solar power plants," Appl. Therm. Eng., **31**(5), pp. 872–879.

[8] Rasouli, R., Narayanan, V., Rasouli, E., and Narayanan, V., 2014, "Single-Phase Cryogenic Flows Through Microchannel Heat Sinks," ASME 2014 12th International Conference on Nanochannels,

Microchannels, and Minichannels, ASME, Chicago, IL, USA, pp. 1–16.

[9] Yao, Z., Wang, Z., Lu, Z., and Wei, X., 2009, "Modeling and simulation of the pioneer 1MW solar thermal central receiver system in China," Renew. Energy, **34**(1), pp. 2437–2446.

[10] Yu, Q., Wang, Z., Xu, E., Li, X., and Guo, M., 2012, "Modeling and dynamic simulation of the collector and receiver system of 1MWe DAHAN solar thermal power tower plant," Renew. Energy, **43**(1), pp. 18–29.

[11] He, Y. L., Cui, F. Q., Cheng, Z. D., Li, Z. Y., and Tao, W. Q., 2013, "Numerical simulation of solar radiation transmission process for the solar tower power plant: From the heliostat field to the pressurized volumetric receiver," Appl. Therm. Eng., **61**(2), pp. 583–595.

[12] Fernández, P., and Miller, F. J., 2015, "Performance analysis and preliminary design optimization of a Small Particle Heat Exchange Receiver for solar tower power plants," Sol. Energy, **112**, pp. 458–468.

[13] Garbrecht, O., Al-Sibai, F., Kneer, R., and Wieghardt, K., 2013, "CFD-simulation of a new receiver design for a molten salt solar power tower," Sol. Energy, **90**, pp. 94–106.

[14] Rymal, C., Apte, A. V., Narayanan, V., and Drost, K., 2013, "Numerical Design of a High-Flux Microchannel Solar Receiver," Proceedings of the ASME 2013 7th International Conference on Energy Sustainability, ASME, Minneapolis, MN, USA, p. V001T11A012.

[15] L'Estrange, T., Truong, E., Rasouli, E., Narayanan, V., Rymal, C., Apte, S., and Drost, K., 2015, "High Flux Microscale Solar Thermal Receiver for Supercritical CO2 Cycles," ASME 2015 13th International Conference on Nanochannels, Microchannels, and Minichannels, ASME, San Francisco, CA, pp. 1–10.

[16] Haynes International, "Haynes ® 230 ® alloy."

[17] Klein, S. A., 2014, "F-Chart Software: EES."

[18] Lemmon, E. E., Jacobsen, R. T., and Penoncello, S. G., 2000, "Thermodynamic Properties of Air and Mixtures Of Nitrogen, Argon, and Oxygen from 60 to 2000 K at Pressure to 2000 MPa," J. Phys. Chem. Ref. Data, **29**(3).

[19] Span, R., and Wagner, W., 1996, "A New Equation of State for Carbon Dioxide Covering the Fluid Region from the Triple-Point Temperature of 1100 K at Pressure up to 800 MPa," J. Phys Chem. Ref. Data, **25**(6).

[20] Bergman, T., Lavine, A., Incropera, F., and Dewitt, D., Introduction to Heat Transfer, John Wiley & Sons, Holboken, NJ.

[21] Kays, W. M., M.E., C., and Weigand, B., 2005, Convection Heat and Mass Transfer, Boston.

[22] Churchill, S. W., and Chu, H. H. S., 1975, "Int. J. Heat an," Int. J. Heat Mass Transf., **18**, p. 1323.

[23] Koşar, A., Mishra, C., and Peles, Y., 2005, "Laminar Flow Across a Bank of Low Aspect Ratio Micro Pin Fins," J. Fluids Eng., **127**(3), p. 419.

[24] Qu, W., and Siu-Ho, A., 2008, "Liquid Single-Phase Flow in an Array of Micro-Pin-Fins—Part I: Heat Transfer Characteristics," J. Heat Transfer, **130**(12), p. 122402.

[25] Zukauskas, A., 1972, "Heat Transfer from Tubes in Cross Flow," Adv. Heat Transf., **8**.

[26] Churchill, S. W., 1977, "Friction factor equation spans all fluid flow regimes," Chem. Eng., **84**(1), pp. 91–82.